

One scalar is all you need - absolute depth estimation using monocular self-supervision

Alexandra Dana

Nadav Carmel

Amit Shomer

Ofer Manela

Tomer Peleg

Samsung

Samsung Israel R&D Center, Tel Aviv, Israel

alex.dana@samsung.com

Abstract

Self-supervised monocular depth estimators can be trained or fine-tuned on new scenes using only images and no ground-truth depth data, achieving good accuracy. However, these estimators suffer from the inherent ambiguity of the depth scale, significantly limiting their applicability. In this work, we present a method for transferring the depth-scale from existing source datasets collected with ground-truth depths to depth estimators that are trained using self-supervision on a newly collected target dataset consisting of images only, solving a significant limiting factor.

We show that self-supervision based on projective geometry results in predicted depths that are linearly correlated with their ground-truth depths. Moreover, the linearity of this relationship also holds when jointly training on images from two different (real or synthetic) source and target domains. We utilize this observed property and model the relationship between the ground-truth and the predicted up-to-scale depths of images from the source domain using a single global scalar. Then, we scale the predicted up-to-scale depths of images from the target domain using the estimated global scaling factor, performing depth-scale transfer between the two domains. This suggested method was evaluated on the target KITTI and DDAD datasets, while using other real or synthetic source datasets, that have a larger field-of-view, other image style or structural content. Our approach achieves competitive accuracy on KITTI, even without using the specially tailored vKITTI or vKITTI2 datasets, and higher accuracy on DDAD, when using both real or synthetic source datasets.

1. Introduction

Monocular depth estimation is a fundamental problem in computer vision with numerous scene understanding applications, such as autonomous driving and navi-

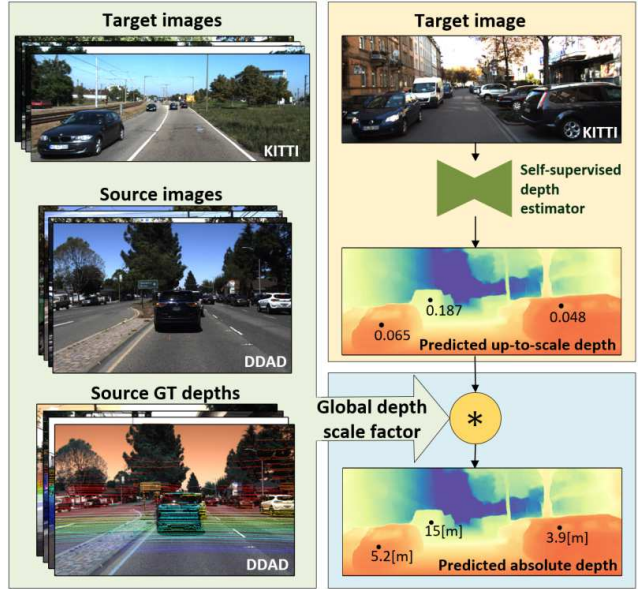


Figure 1. Applying depth-scale transfer from a source domain to a target domain on an MDE that is trained using self-supervision. Left: the MDE is trained on images from both the source and the target domains using self-supervision. A global depth scaling factor is calculated for the trained MDE, using the source estimated up-to-scale depths and their GT depth measurements. Right: during inference, up-to-scale depths are inferred on images from the target domain. These are scaled to absolute depths using the estimated global depth scaling factor.

gation [16, 45, 37, 13], robotics [31, 11, 40] and augmented reality [10, 29]. Current methods for training CNN-based Monocular Depth Estimators (MDE) include two major methodologies: full-supervision and self-supervision. Fully-supervised [14, 33, 4, 20] or semi-supervised [32, 1, 23, 3] models are trained using ground-truth (GT) depth that is measured directly by LiDARs or reconstructed using a stereo setting [30, 43, 38, 9]. Although training models with

GT depth measurements enables predicting *absolute* depth, fine-tuning such models on new scenes requires collecting images and their corresponding depth measurements, complicating the data collection setup with additional depth sensors or cameras, increasing setup complexity and costs [11].

Thus, multiple efforts [50, 18, 19, 44, 22, 8] were invested to improve the self-supervised training regime, to enable training or fine-tuning MDEs using only images. In this approach, two images acquired at different times are used to predict the depth of one image using projective geometry [27]. Due to the nature of this training, the scale of the predicted depth is ambiguous [27]. In this work we refer to predicted depths using this method as *up-to-scale* depths. This major weakness limits its use in real-world applications such as autonomous driving, navigation and robotics, that require absolute depth-scale values.

In this work, we confront this self-supervised training limitation by presenting a method to *transfer* the *depth-scale* from existing datasets that were collected with GT depths, to self-supervised models that are trained on newly-collected datasets lacking these measurements. The new data may have a different style or structural content, and be collected by a camera with a different field-of-view (FOV). The proposed method enables training or fine-tuning a self-supervised MDE on only new images, while enabling it to predict absolute depths.

We start by showing that although models trained using projective geometry based losses can predict only up-to-scale depths, these predictions are *linearly* correlated with their respective GT depths, not only per a single image, but also across multiple images, displaying *global* linear correlation characteristics, a property which we refer to in this work as *linear depth ranking*.

Moreover, we show that when adjusting images from two different domains to a single FOV, under the assumption of similar camera heights, training the MDE on images from two domains achieves *cross-domain linear depth ranking*, regardless of possible domain gaps [25, 48], and without using additional intermediate tasks [24]. Furthermore, we demonstrate this property when mixing (1) real and real or (2) synthetic and real data, which was collected using cameras with different FOVs.

Finally, this observation led us to hypothesize that if self-supervised training resulted in linear depth ranking across two datasets collected from two different domains, then depth-scale properties from one domain could be transferred to another. Let us define a dataset collected with GT depth as the *source* domain and another dataset collected without it as the *target* domain. Then the relationship between the absolute and the predicted up-to-scale depths in the source domain could be *transferred* to the target domain, achieving *depth-scale transfer* between them.

In this work, we show for the first time that such a depth-

scale correction factor can be globally approximated using a *single scalar* (see Figure 1), thus not increasing the computational complexity of the MDE. We demonstrate this method on both KITTI [17] and DDAD [21] automotive datasets using various real and synthetic source datasets, achieving highly competitive or better accuracy with respect to other online depth-scale methods, weakly-supervised or mixed-supervised training regimes.

2. Previous works

MDEs can be trained using full or semi-supervision with LiDAR [32, 14, 33, 23, 20, 4] or other absolute depth measurements [30, 43, 38, 9]. These models currently achieve state-of-the-art depth estimation accuracy. However, such training regimes require collecting additional GT depth measurements to enable fine-tuning the model on new scenes. To overcome this limitation, MDEs can also be trained in a self-supervised manner using two or more RGB images, with losses that reflect projective geometry principles [50, 18, 21]. Although these methods achieve competitive up-to-scale depth accuracy and enable fine-tuning on new data without collecting new GT depth measurements, they are lacking world-related scaling.

Over the years, various solutions were suggested to overcome this inherent self-supervision limitation. Some studies used weak-supervision on the target data to regularize the predicted depth-scale values by using the measured car velocity [21], its GPS location [7] or IMU measurements [47] (regularizing depth via the relative translation between frames in absolute units). However, such setups require additional signals acquisition for the newly collected data.

Online depth-scaling of predicted up-to-scale depth *per image* was suggested by using the known camera height and online estimation of the road plane [36, 46]. However, such a method requires sufficient visible free road to estimate its plane, which is not always possible in jammed scenes or turns, and also assumes the road is perfectly flat. Our solution does not explicitly depend on such assumptions.

Various works also developed methods for transferring the depth-scale from existing source datasets to a new target domain. To overcome difficulties arising from training the MDE on source and target images with different FOVs, these solutions used synthetic data for the source domain, created with the same intrinsics, extrinsics and even similar geometrical structures as in the target domain, such as vKITTI [15] and vKITTI2 [5], for the target KITTI dataset. Since real and synthetic data still differ in style, initial attempts focused on closing these gaps using style transfer from the target to the source domain [2, 49, 48]. Recent solutions trained on such synthetic and real datasets [26, 24, 35, 41] used mixed-supervision, where the MDE was self-supervised using images from both domains and also fully-supervised using the source GT depth,

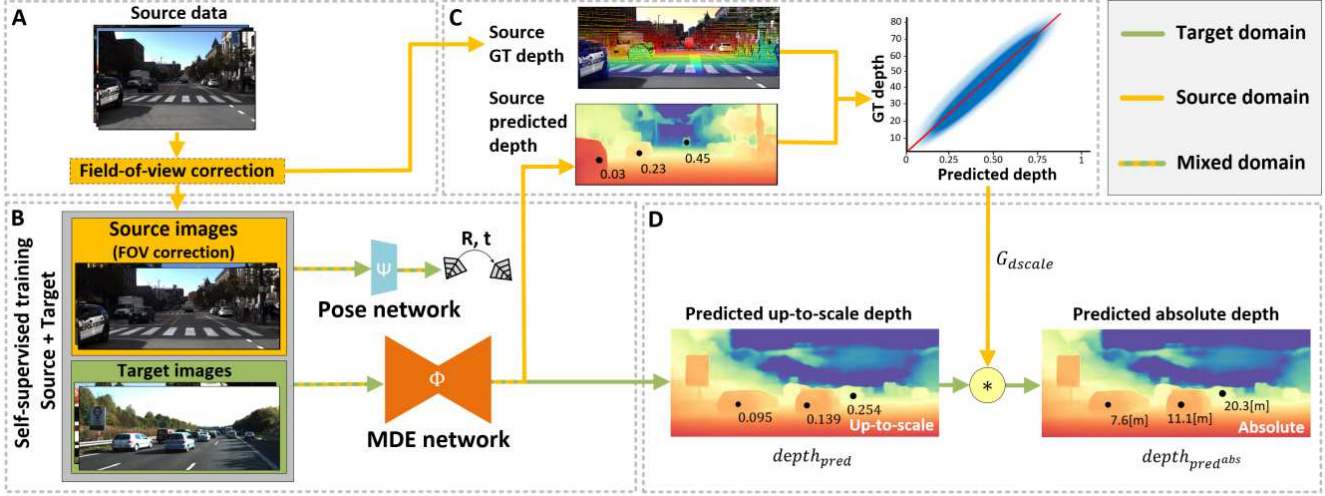


Figure 2. General architecture. (A) The FOV of data from the source domain is corrected to the target FOV. (B) The depth and pose networks are trained using self-supervision on both source and target training images (mixed batches). (C) Data from the source domain is used to generate the GT vs. predicted up-to-scale mapping. A linear model is used to fit it, resulting in a global slope G_{dscale} . (D) Estimated target up-to-scale depths are multiplied by the estimated global depth-scale factor G_{dscale} , resulting in absolute depth predictions.

thus tightly coupled between the depth ranking and scaling. In addition, some solutions used additional intermediate tasks such as semantic segmentation [24] or introduced an additional network to predict the depth-scale [41].

A recent work [35] demonstrated depth-scale transfer between two real domains by controlling for the style differences. However, in that work the FOV properties of the datasets were ignored, breaking the geometrical consistency between the domains.

Differently, in this work we present new insights about self-supervised MDEs. We use these properties to fully decouple between the depth ranking module that is trained using only self-supervision and the depth scaling module that uses source GT depths. We also demonstrate that the depth-scale can be transferred from various data source types with different FOVs, without making any style or structural assumptions. In addition, we do not use any additional intermediate tasks nor add additional networks, thus preserving the initial MDE computational complexity.

3. Methods

3.1. Self-supervised training an MDE model

Training an MDE using self-supervision aims at reconstructing the view from an image collected at time $t \pm 1$ from an image collected at time t , using the estimated depth from the image at time t and the estimated relative pose between the frames [50, 18]. Let us denote by Φ a network that receives as input an image I_t and by d_t its estimated up-to-scale depth output, and by $T_{t \rightarrow t \pm 1}$ the relative pose between two frames I_t and $I_{t \pm 1}$ estimated by a network Ψ . Given

the camera intrinsics K , a homogeneous pixel $p_t \in I_t$ can be mapped to a homogeneous pixel $p_{t \pm 1} \in I_{t \pm 1}$ as follows [27]:

$$\hat{p}_{t \pm 1} \sim K \hat{T}_{t \rightarrow t \pm 1} d_t(p_t) K^{-1} p_t \quad (1)$$

3.2. Matching the field-of-view of the source dataset to the target domain

Training an MDE on images collected using different camera FOVs (real or synthetic) introduces significant geometrical differences that a naïve self-supervised training regime cannot easily compensate for. However, the majority of the publicly available datasets for autonomous driving are collected using cameras with different FOVs (see Section 3.8). To enable self-supervised training on mixed batches of images collected with sensors of different FOVs without breaking the scene geometrical consistency, we adjusted the FOV of the source images to the FOV of the target images, resulting in training data with homogeneous FOV and aspect ratio. The FOV of a camera is calculated as:

$$\angle \frac{FOV}{2} = \text{atan} \left(\frac{w}{2f} \right) \quad (2)$$

where f is the focal length of the camera and w is the width of the image, both in pixel units. Let us denote the camera focal length and the image width in the target domain by f_T and w_T respectively. Let us denote the camera focal length in the source domain by f_S . To adjust the FOV of the source images to the target FOV, we cropped the image width w_S to $w_{S \rightarrow T}$, as follows (assuming $f_S < f_T$):

$$\angle \frac{FOV_T}{2} = \text{atan} \left(\frac{w_T}{2f_T} \right) = \text{atan} \left(\frac{w_{S \rightarrow T}}{2f_S} \right) \quad (3)$$

resulting in:

$$w_{S \rightarrow T} = w_T \frac{f_S}{f_T} \quad (4)$$

The crop height was then calculated using the target image aspect ratio. Finally, the image crop was resized to the target image size using a bilinear interpolation to enable training on mixed batches. The same process was applied to the source sparse GT map, using nearest-neighbor interpolation. In case where $h_{S \rightarrow T}$ is higher than h_T , the crop was extended, as described in the Supplementary methods.

3.3. Estimating the depth scaling factor using a global estimator

We started by inferring the trained MDE Φ on the *source* test dataset and then analyzed the relationship between the GT and the predicted up-to-scale depths $depth_{pred}$. Since the training regime was designed to predict depths without any offset (see Section 3.5), we expected zero-depth predictions to match zero absolute depth. The GT and the predicted up-to-scale depth scatter plot indicated a linear *global* relationship (see Section 4.1) across the evaluated dataset, thus in this work we chose to model this relationship using a linear fitting with G_{dscale} slope and zero intercept:

$$depth_{GT}^i \cong G_{dscale} \cdot depth_{pred}^i \quad (5)$$

where G_{dscale} is calculated as:

$$G_{scale} = \frac{\text{median}(depth_{GT}^{i,j})}{\text{median}(depth_{pred}^{i,j})} \quad (6)$$

The $\text{median}(\cdot)$ is applied on up-to-scale depth predictions (or GT depth values) from all images i in the source test dataset and j are pixels existing GT depth. This simplistic model of G_{scale} was designed to filter out outliers in a stable manner, as shown in Section 4.

3.4. Overall overview of the depth-scale-transfer methodology

First, we adjusted the FOV of the source domain data (train and test splits) to match the FOV of the target domain, as described in Section 3.2 and Figure 2A. Training images from both source and target domains were randomly split into batches of four and networks Φ and Ψ were trained as described in Section 3.5 and Figure 2B.

Next, we used the depth network Φ to infer the up-to-scale depths of images from the *source* test dataset. We fit the relationship between these predictions and their respective GT depths as described in Section 3.3 and Figure 2C.

Finally, to estimate absolute depths on the *target* domain, we inferred the up-to-scale depth of images from the target test dataset using the depth network Φ and multiplied the resulting up-to-scale depths by G_{dscale} , obtaining target absolute depth predictions $depth_{predabs}^i$ (see Figure 2D):

$$depth_{predabs}^i = G_{dscale} \cdot depth_{pred}^i \quad (7)$$

3.5. Training methodology additional details

In this work we adopted the Φ, Ψ architectures presented in Monodepth2 [18], but replaced the backbone of the depth network Φ with MobileNetV2 [39] instead of the original ResNet18 [28]. The MDE was trained using a photometric loss [18] for 15 epochs, with a learning rate of 10^{-4} , and for another five epochs with a learning rate of 10^{-5} .

Self-supervised MDEs are highly sensitive to local motion, since the scene stationarity assumption is broken on moving objects, invalidating Eq. (1) on such regions. This weakness causes poorly estimated depths on moving objects such as vehicles, reducing the overall depth accuracy. Previous efforts to correct this phenomenon included filtering vehicles that moved with the same velocity as the ego-motion [18]. Others regularized the loss by using additional optical flow predictions [22], applied separate regularization for static and dynamic objects [6, 34] or fully-supervised these regions with GT depth [44]. In this study we significantly reduced this phenomenon by creating additional local motion masks, as described in the Supplementary material.

In the original work [18], the authors used the depth network Φ to estimate the inverse depth, then they inverted the prediction and scaled it to depth values of [0.1, 80] per image to avoid shrinking of the estimated depth. This correction introduces a bias, which we avoided in this work, by directly predicting up-to-scale depths. The predicted up-to-scale depth range is between 0 and 1, as determined by the last sigmoid activation of the Φ decoder. We demonstrated that this implementation achieves similar accuracy, while providing simpler interpretability, which was used for additional analyses, as shown in Section 4.

3.6. Estimating the per-image depth scaling factor using an alternative CNN network

A recent work [41] implemented depth-scale transfer using a convolutional network that receives as input features from the last layer of the depth decoder network and was trained to estimate the depth-scale factor *per image*. To compare our global estimation approach to a depth scaling factor *per image* approach, we also implemented a convolutional neural network Γ . The global scaling model receives as input the up-to-scale depth map, thus for a fair comparison, network Γ was also designed to receive as input up-to-scale depth maps. We implemented the network using a MobileNetV2 architecture [39] and converted its head into a regression head. The network was trained to regress for *each* input up-to-scale depth map $depth_{pred}^i$ its depth-scale correction factor net_{dscale}^i , such that:

$$depth_{predabs}^i = net_{dscale}^i \cdot depth_{pred}^i \quad (8)$$

Up-to-scale depth maps were inferred on images from the source train dataset and used as inputs to train network Γ . The network was trained for 15 epochs in a fully-supervised manner using L1 loss between the predicted $depth_{pred}^i$ (see Eq. (8)) and the absolute depth $depth_{GT}^i$ values, with a learning rate of 10^{-4} . We used the *source* test dataset to select the epoch with the lowest *AbsRel* (see Section 3.9) and reported the selected model accuracy on the *target* test dataset.

3.7. Estimating the absolute depth using full-supervision

To enable comparison of our absolute depth predictions to predictions of a similar architecture trained in a fully-supervised manner, the depth network Φ was trained directly on images and GT depth measurements from the *target* train dataset, using an L1 loss between the predicted and the GT depth values [30]. The model was trained for 15 epochs with a learning rate of 10^{-4} , and for another five epochs using a learning rate of 10^{-5} .

3.8. Datasets

KITTI. This dataset [15] is considered the standard benchmark for depth evaluation. The front cameras have a FOV of 81° and are located 1.65 m above the ground.

DDAD. This benchmark [21] was collected using six cameras. The front and rear cameras have a FOV of $47^\circ/83^\circ$ and are located 1.55 m above the ground. In this report we referred to data collected using the front and rear cameras as DDAD1 and DDAD9 respectively, following the dataset camera numbering convention (we used data from various cameras to meet the $f_S < f_T$ assumption).

vKITTI2. This dataset [5] was recently released as a more photo-realistic version of vKITTI [15]. The camera has a FOV of 81° and is located 1.58 m above the ground.

The DDAD1 and the KITTI datasets were used as target domains. For the DDAD1 target domain we used KITTI and vKITTI2 as source domains. For the KITTI target domain we used vKITTI2 and DDAD9 as source domains (the DDAD1 FOV is too small with respect to the KITTI FOV). The used train and test data splits and additional data details can be found in the Supplementary material.

3.9. Depth evaluation metrics

We evaluated the accuracy of the predicted depths by using various standard metrics [12]. Specifically, to measure the accuracy of the predicted absolute depth values, we used the absolute relative depth accuracy (*AbsRel*) metric, without applying any normalization to the predicted depths. To estimate the accuracy of the predicted up-to-scale depths, those were normalized first using the ratio between the median of the predicted and the GT depth values (per image) [50], resulting in *AbsRel_{norm}*.

To assess scaling similarity to GT, we also calculated the median ratio between the GT and the predicted absolute depths per image, and then averaged this value across the entire test dataset, resulting in *scale_{ratio}*. More details on these metrics can be found in the Supplementary material.

4. Results

4.1. Studying the relationship between GT and predicted up-to-scale depths

We started our analysis by separately training the MDE on training datasets from various domains. For each trained model we plotted and analyzed the relationship between the GT and the predicted up-to-scale depths on its respective test dataset, as seen in Figure 3A. The linearity of this relationship was measured by the Pearson correlation coefficient, resulting in values bigger than 0.80 (see Table 1).

During training, no additional bias corrections were applied to the network output (see Section 3.5), thus we expected GT values close to zero to be mapped to predicted up-to-scale depths close to zero (*i.e.* zero offset). Indeed, the results in Figure 3A demonstrate this assumption. Therefore, for each evaluated test dataset we fit the GT to up-to-scale depths using the linear model described in Section 3.3 and reported the G_{dscale} factor in Table 1. Calculated G_{dscale} values showed a high variability among the evaluated datasets, thus cannot be straightforwardly transferred among domains.

A closer examination of the scatter plots in Figure 3A reveals that some measurements are outside of the main linear trend. We hypothesized that these outliers could result from poor predictions of the MDE. To validate this assumption we filtered out predicted values with $AbsRel_{norm} > 15\%$. As seen in Figure 3B, the filtering indeed removed the majority of outliers. Moreover, the Pearson correlation coefficient increased to above 0.97, reinforcing our observation that MDEs trained using self-supervision can *globally* linearly rank depth values across images, and not only linearly rank the depths within a specific image.

We postulated that the observed linearity results from the training loss which implements projective geometry, regardless of the network architecture. To validate this assumption, we also analyzed up-to-scale predictions of a significantly different architecture, PackNet [21], which uses 3D convolutions and a different encoder-decoder architecture, but trained with a similar loss. As shown in Figure S3 (Supplementary material), the predicted up-to-scale depths of this self-supervised MDE are also linearly correlated to the GT depths, reinforcing this assumption.

Previous studies [36, 38] modeled this relationship *per image*. To compare to this approach, we also modeled the GT to predicted up-to-scale depth per image using our linear model. Figure 3C indeed shows that the obtained slopes

Target	All predictions			Predictions with $AbsRel_{norm} < 15\%$			
	G_{dscale}	Pearson coefficient	I_{dscale}	Remaining pixels	G_{dscale}	Pearson coefficient	I_{dscale}
KITTI	84.3	0.93	85.2 ± 6.7	83.6%	83.1	0.98	85.2 ± 6.1
vKITTI2	116.1	0.80	118.0 ± 12.9	61.1%	116.7	0.98	117.1 ± 8.5
DDAD1	126.2	0.97	126.5 ± 11.0	77.6%	126.8	0.98	125.8 ± 10.4
DDAD9	119.8	0.85	122.7 ± 15.0	59.9%	119.9	0.97	122.1 ± 14.7

Table 1. Relationship between the GT and the predicted up-to-scale depths. Our MDE was separately trained on various datasets using self-supervision. Calculations were done on their test datasets, using all predictions or predictions with $AbsRel_{norm} < 15\%$ (remaining pixels % after the filtering is mentioned in the fifth column). For each data slicing the G_{dscale} value and the Pearson correlation coefficient was calculated. In addition, the GT to predicted up-to-scale depth relationship was separately fitted *per image* using the linear model described in Section 3.3. Its mean and standard deviation across all test images is reported in the I_{dscale} column.

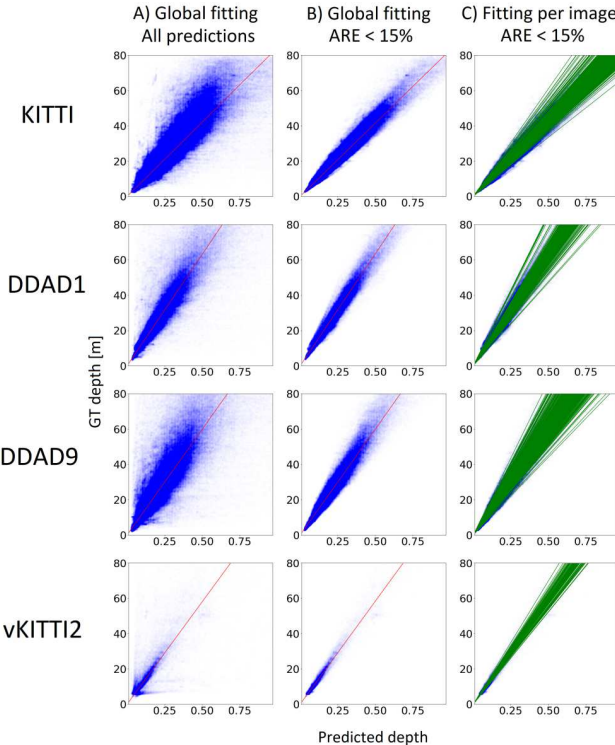


Figure 3. Scatter plots of the GT vs. the predicted up-to-scale depth values. Our MDE was separately trained on various datasets using self-supervision and inferred on test images from the same domain. (A) All test data. The red line depicts the linear global fit applied on all data (see Eq. (5)). (B) Predictions with $AbsRel_{norm} > 15\%$ were filtered out and the fitting was recalculated. (C) The GT vs. the predicted depth relationship was similarly linearly fitted *per image* and depicted by different green lines.

vary across images, but that their mean across images is comparable to the global slope G_{dscale} (see Table 1).

We hypothesize that this variability could be explained by imperfect convergence due to non-optimal training losses, architecture capacity, image quality, generalization gaps and other factors. Conducting experiments to mea-

sure the impact of each factor on the slope variability across images is beyond the scope of this work; however, Table 1 shows that when removing poor predictions ($AbsRel_{norm} > 15\%$), this variability also decreased, supporting this assumption.

Although the empirical results indicated of exiting slope variability across images, since the obtained mean of the slopes is similar to G_{dscale} and their variability is substantially smaller than their mean, in this work we evaluated how well a single *global* depth scaling factor could be used to model the relationship between the GT and the predicted up-to scale depths.

4.2. Training the MDE on images from two domains

Modeling the GT to predicted up-to-scale depth relationship resulted in highly varying G_{dscale} values for different domains (see Table 2, third column). Thus, even if a self-supervised MDE is able to linearly rank depths, the modeled G_{dscale} is not transferable to other domains. To demonstrate that G_{dscale} differences cannot be explained only by different FOVs, an additional MDE was separately trained on source datasets after adjusting the source images to match the target FOV (see Table 2, fourth column), showing that this step on its own is insufficient.

To overcome the G_{dscale} high differences between each pair of domains, we hypothesized that jointly self-supervised training the MDE on both the source and the target datasets could potentially result in ranking the depths of both domains on a *common* scale, thus achieving a *de facto* inter-domain depth ranking. To enable training on two domains, images from the source dataset were adjusted to the FOV of the target domain, as described in Section 3.2. The fifth column in Table 2 shows that training the MDE on data from two domains resulted in similar G_{dscale} slopes for both the source and the target test datasets, suggesting that the calculated G_{dscale} on the source data could be applied also on the target data.

To evaluate the impact of training the MDE on data from an additional domain on the depth estimation accu-

Test domain	Type	G_{dscale} (ARE<15%)		
		Separate trainings	Separate trainings $S \xrightarrow{\text{FOV}} T$	Single training $S \xrightarrow{\text{FOV}} T$
KITTI	T	83.1	83.1	99.8
DDAD9	S	119.9	105.9	99.1
KITTI	T	83.1	83.1	102.1
vKITTI2	S	116.1	116.1	104.4
DDAD1	T	126.8	126.8	98.7
KITTI	S	83.1	69.3	93.0
DDAD1	T	126.8	126.8	122.9
vKITTI2	S	116.1	133.7	125.1

Table 2. Estimated G_{scale} values on various test datasets (first column). Second column indicates which dataset was used as source (S) or target (T). Third column: two MDEs were trained separately on the source and the target training datasets; Fourth column: two MDEs were trained separately on the source and the target training datasets, the source images were adjusted to the target FOV ($S \xrightarrow{\text{FOV}} T$); Fifth column: a single MDE was trained on a mixture of training data from the target and the source domains after the source images were adjusted to the target FOV.

racy of the target domain, we also trained the MDE using self-supervision directly on the target domain. The similar $AbsRel_{norm}$ values in Table 3 (fourth and last columns), indicated that self-supervised training on two domains (after aligning the source FOV to the target FOV) did not deteriorate the depth estimation accuracy on the target domain.

4.3. Transferring the global depth scaling factor from the source to the target domain

To evaluate the suggested depth-scale transfer method, we trained the MDE on various dataset pairs (see Table 3) and calculated G_{dscale} on the source test dataset. Then we inferred up-to-scale depths on target images from the test dataset and scaled them using G_{dscale} , resulting in absolute target depth predictions (see Section 3.4). We report $AbsRel$ of these predictions in Table 3 (third column). Additional depth-accuracy metrics, as well as visual examples of the estimated depth maps can be found in the Supplementary material. These results indicate that our single scalar estimator was able to transfer the depth-scale from both *real* and *synthetic* datasets for both KITTI and DDAD target datasets, achieving an $AbsRel$ of 8.4% for KITTI and 12.8% for the DDAD1 dataset. The mean predicted depth deviated on average by less than 5% with respect to the GT depth (see $scale_{ratio}$ in the fifth column of Table 3), demonstrating the accuracy of our method.

To further analyze our method’s accuracy, we also trained the MDE model Φ directly on the training target dataset using full-supervision (see Section 3.7). For KITTI and DDAD1 this training regime achieved an $AbsRel$ of

7.9% and 10.0% respectively (see Table 3), showing that our depth-scale transfer method is competitive with fully-supervised methods that directly use GT depth measurements, when controlling for the same network architecture.

$AbsRel_{norm}$ is agnostic to the depth scaling estimation quality, thus reflects errors related to other factors such as the limited capacity of the network, insufficient loss regularization, poor image quality and domain gaps due to limited training data, *etc.* The results in Table 3 (third *vs.* fourth columns) indicate of a small difference between the $AbsRel$ and the $AbsRel_{norm}$, providing an additional metric to quantify our depth-scale related error.

To enable training on mixed batches, source images were resized to match the size of target images. To evaluate the effect of incorrect source image resizing, we implemented two naïve alternatives that do not consider the FOV of images: in the first option (A), source images were centered to target images and cropped to match their size; in another alternative (B), source images were resized to the target images size (width wise), and then were cropped to match the target height. We applied these methods when using DDAD as a source domain to the KITTI target domain, and then repeated the self-supervised training using mixed batches, calculated the G_{dscale} and applied depth-scale transfer. The results in Table 4 show that although the $AbsRel_{norm}$ is comparable to $AbsRel_{norm}$ of our FOV adjustment method, the $AbsRel$ was significantly higher. This indicates that resizing source images without taking into consideration the target FOV, fails to enable correct depth-scale transfer using the suggested method.

Finally, we compared our method to others (see Table 5) and achieved a lower $AbsRel$ on both KITTI and DDAD1 target domains [35, 24] when using real source datasets that were not specifically tailored to them, by only using a single depth-scaling factor. We also achieved competitive or better accuracy to other depth-scale-transfer methods that used specially tailored synthetic data for KITTI [26, 24, 35, 41] and DDAD [24], and also showed that vKITTI2 can be successfully used as a source to other real datasets such as DDAD. Our accuracy is also competitive to weakly-supervised methods that used target GT velocity [21], GPS [7] or IMU [47] during training, and to on-line depth scaling methods [36, 46] that require road visibility during inference. Models that significantly exceeded our accuracy were fully-supervised on the target domain [33, 20], used heavier architectures (ours has 4.7M parameters while PackNet [20] has 128M parameters) or were trained with specialized losses [33].

4.4. Estimating the depth-scale factor per image using a CNN network

To compare our suggested model to a CNN based approach [41], we also implemented a dedicated network Γ

Target	Source	Global scaling scalar G_{dscale} (ours)			Per-image scaling network Γ (ours)			Fully-sup.	Self-sup.
		$AbsRel$	$AbsRel_{norm}$	$scale_{ratio}$	$AbsRel$	$AbsRel_{norm}$	$scale_{ratio}$	$AbsRel$	$AbsRel_{norm}$
KITTI	DDAD9	0.084	0.076	1.03 ± 0.05	0.091	0.075	0.97 ± 0.06	0.079	0.087
	vKITTI2	0.096	0.077	1.04 ± 0.06	0.101	0.076	1.05 ± 0.06		
DDAD1	KITTI	0.128	0.119	0.95 ± 0.05	0.135	0.118	0.94 ± 0.06	0.100	0.120
	vKITTI2	0.137	0.135	1.01 ± 0.05	0.169	0.134	1.08 ± 0.07		

Table 3. Comparing the accuracy of our suggested depth-scale transfer methods to other training regimes for the KITTI [42] and the DDAD [21] target datasets. Both our depth-scale transfer methods use as input up-to-scale depth predictions of an MDE that was trained using self-supervision on a mix of images from the source and target datasets. The fully-supervised and self-supervised models in the last two columns are trained directly on the train set of the target.

Resizing method	Type	Domain	Slope	$AbsRel$	$AbsRel_{norm}$
A	S	DDAD9	97.08	0.423	0.094
	T	KITTI	70.51		
B	S	DDAD1	163.63	0.847	0.084
	T	KITTI	86.69		

Table 4. Alternative source image resizing implementations to match the target image size. Second column indicates the used source (S) and target (T) datasets for training on both domains. The slopes are calculated using the G_{dscale} model.

Target	Method	Ref.	Source	$AbsRel$		
				[12]	[42]	[21]
KITTI	Full-sup	[20]	-	0.052	-	-
		[33]	-	0.059	-	-
	Weak-sup	[21]	-	0.103	0.075	-
		[47]	-	0.108	-	-
		[7]	-	0.112	0.088	-
	OnlineS	[36]	-	0.113	-	-
		[46]	-	0.118	-	-
	DST	[35]	CS	0.119	-	-
		[35]	vKITTI	0.120	-	-
		[26]	vKITTI	0.104	-	-
		[24]	vKITTI2	0.107	-	-
		[41]	vKITTI2	0.109	-	-
		Ours	vKITTI2	0.112	0.096	-
		Ours	DDAD9	0.111	0.084	-
DDAD1	Full-sup	[20]	-	-	-	0.083
	DST	[24]	PD	-	-	0.147
		Ours	KITTI	-	-	0.128
		Ours	vKITTI2	-	-	0.137

Table 5. Comparing our global depth-scale transfer (DST) accuracy to fully-supervised (Full-sup) and weakly supervised (Weak-sup) methods that were trained directly on the target domain. We also compared to other DST methods that use the source GT depth and to online scaling (OnlineS) methods. CS and PD are abbreviations of Cityscapes and Parallel Domain. References in the $AbsRel$ columns indicate the used evaluation dataset.

for inferring depth-scale *per image* from up-to-scale depth maps (see Section 3.6). Table 3 shows that when given the same input information, a network with 3.5M parameters achieved similar or lower accuracy as the single scalar global factor G_{dscale} method. Future directions might include specialized losses for improving the per-image accuracy of such a solution.

5. Discussion

In this work we confronted a significant weakness of MDEs trained using self-supervision by leveraging the depth ranking linearity of such a training regime. We suggested using a single scaling factor for correcting up-to-scale predicted depths to absolute depths, without altering the architecture of the MDE, nor adding additional computation complexity.

The suggested method was implemented using a relatively lite MDE architecture with a standard self-supervised training loss. In addition, our design totally decoupled between the depth ranking and the depth scaling tasks. Thus, more advanced architectures and losses can independently improve the baseline performance of the self-supervised training, that directly affects the depth ranking accuracy. This in turn impacts also the absolute depth predictions, even when using an ideal depth-scaling factor. We postulate that more accurate self-supervised MDEs can also reduce the variability of the GT to up-to-scale relationship across images, thus enabling a better generalization of the single depth-scale correction factor.

We demonstrated our method on two highly popular automotive datasets and showed that the depth-scale correction factor could be transferred from both real and synthetic datasets, emphasizing the insensitivity of this approach to style or structural domain gaps.

The suggested method enables training MDEs for predicting absolute depth from images only, collected using the same or new sensors with different FOVs, by reusing existing data. This solution is highly applicative for continuous learning from dynamic scenes, where depth models can require frequent adjustments, without the need to collect ad-

ditional GT depth measurements, that can complicate the sensors setup and increase costs.

References

- [1] Ali Jahani Amiri, Shing Yan Loo, and Hong Zhang. Semi-supervised monocular depth estimation with left-right consistency using deep neural network. In *2019 IEEE International Conference on Robotics and Biomimetics (ROBIO)*, pages 602–607. IEEE, 2019.
- [2] Amir Atapour-Abarghouei and Toby P Breckon. Real-time monocular depth estimation using synthetic data with domain adaptation via image style transfer. In *Proceedings of the IEEE conference on computer vision and pattern recognition*, pages 2800–2810, 2018.
- [3] Jongbeom Baek, Gyeongnyeon Kim, and Seungryong Kim. Semi-supervised learning with mutual distillation for monocular depth estimation. In *2022 International Conference on Robotics and Automation (ICRA)*, pages 4562–4569. IEEE, 2022.
- [4] Shariq Farooq Bhat, Ibraheem Alhashim, and Peter Wonka. Adabins: Depth estimation using adaptive bins. In *Proceedings of the IEEE/CVF Conference on Computer Vision and Pattern Recognition*, pages 4009–4018, 2021.
- [5] Yohann Cabon, Naila Murray, and Martin Humenberger. Virtual kitti 2, 2020.
- [6] Vincent Casser, Soeren Pirk, Reza Mahjourian, and Anelia Angelova. Depth prediction without the sensors: Leveraging structure for unsupervised learning from monocular videos. In *Proceedings of the AAAI conference on artificial intelligence*, volume 33, pages 8001–8008, 2019.
- [7] Hemang Chawla, Arnav Varma, Elahe Arani, and Bahram Zonooz. Multimodal scale consistency and awareness for monocular self-supervised depth estimation. In *2021 IEEE International Conference on Robotics and Automation (ICRA)*, pages 5140–5146. IEEE, 2021.
- [8] Xingyu Chen, Thomas H Li, Ruonan Zhang, and Ge Li. Frequency-aware self-supervised monocular depth estimation. In *Proceedings of the IEEE/CVF Winter Conference on Applications of Computer Vision*, pages 5808–5817, 2023.
- [9] Jaehoon Cho, Dongbo Min, Youngjung Kim, and Kwanghoon Sohn. Deep monocular depth estimation leveraging a large-scale outdoor stereo dataset. *Expert Systems with Applications*, 178:114877, 2021.
- [10] Catherine Diaz, Michael Walker, Danielle Albers Szafir, and Daniel Szafir. Designing for depth perceptions in augmented reality. In *2017 IEEE international symposium on mixed and augmented reality (ISMAR)*, pages 111–122. IEEE, 2017.
- [11] Xingshuai Dong, Matthew A Garratt, Sreenatha G Anavatti, and Hussein A Abbass. Towards real-time monocular depth estimation for robotics: A survey. *IEEE Transactions on Intelligent Transportation Systems*, 23(10):16940–16961, 2022.
- [12] David Eigen, Christian Puhrsch, and Rob Fergus. Depth map prediction from a single image using a multi-scale deep network. *Advances in neural information processing systems*, 27, 2014.
- [13] João M Faria and António HJ Moreira. Implementation of an autonomous ros-based mobile robot with ai depth estimation. In *IECON 2021–47th Annual Conference of the IEEE Industrial Electronics Society*, pages 1–6. IEEE, 2021.
- [14] Huan Fu, Mingming Gong, Chaohui Wang, Kayhan Battamghelich, and Dacheng Tao. Deep ordinal regression network for monocular depth estimation. In *Proceedings of the IEEE conference on computer vision and pattern recognition*, pages 2002–2011, 2018.
- [15] A Gaidon, Q Wang, Y Cabon, and E Vig. Virtual worlds as proxy for multi-object tracking analysis. In *CVPR*, 2016.
- [16] Ravi Garg, Vijay Kumar Bg, Gustavo Carneiro, and Ian Reid. Unsupervised cnn for single view depth estimation: Geometry to the rescue. In *Computer Vision–ECCV 2016: 14th European Conference, Amsterdam, The Netherlands, October 11–14, 2016, Proceedings, Part VIII 14*, pages 740–756. Springer, 2016.
- [17] Andreas Geiger, Philip Lenz, Christoph Stiller, and Raquel Urtasun. Vision meets robotics: The kitti dataset. *The International Journal of Robotics Research*, 32(11):1231–1237, 2013.
- [18] Clément Godard, Oisin Mac Aodha, Michael Firman, and Gabriel J Brostow. Digging into self-supervised monocular depth estimation. In *Proceedings of the IEEE/CVF International Conference on Computer Vision*, pages 3828–3838, 2019.
- [19] Ariel Gordon, Hanhan Li, Rico Jonschkowski, and Anelia Angelova. Depth from videos in the wild: Unsupervised monocular depth learning from unknown cameras. In *Proceedings of the IEEE/CVF International Conference on Computer Vision*, pages 8977–8986, 2019.
- [20] Vitor Guizilini, Rares Ambrus, Wolfram Burgard, and Adrien Gaidon. Sparse auxiliary networks for unified monocular depth prediction and completion. In *Proceedings of the IEEE/CVF Conference on Computer Vision and Pattern Recognition*, pages 11078–11088, 2021.
- [21] Vitor Guizilini, Rares Ambrus, Sudeep Pillai, Allan Raventos, and Adrien Gaidon. 3d packing for self-supervised monocular depth estimation. In *Proceedings of the IEEE/CVF conference on computer vision and pattern recognition*, pages 2485–2494, 2020.
- [22] Vitor Guizilini, Kuan-Hui Lee, Rareş Ambruş, and Adrien Gaidon. Learning optical flow, depth, and scene flow without real-world labels. *IEEE Robotics and Automation Letters*, 7(2):3491–3498, 2022.
- [23] Vitor Guizilini, Jie Li, Rares Ambrus, Sudeep Pillai, and Adrien Gaidon. Robust semi-supervised monocular depth estimation with reprojected distances. In *Conference on robot learning*, pages 503–512. PMLR, 2020.
- [24] Vitor Guizilini, Jie Li, Rareş Ambruş, and Adrien Gaidon. Geometric unsupervised domain adaptation for semantic segmentation. In *Proceedings of the IEEE/CVF International Conference on Computer Vision*, pages 8537–8547, 2021.
- [25] Xiaoyang Guo, Hongsheng Li, Shuai Yi, Jimmy Ren, and Xiaogang Wang. Learning monocular depth by distilling cross-domain stereo networks. In *Proceedings of the Euro-*

pean Conference on Computer Vision (ECCV), pages 484–500, 2018.

[26] Akhil Gurram, Ahmet Faruk Tuna, Fengyi Shen, Onay Urfalioglu, and Antonio M López. Monocular depth estimation through virtual-world supervision and real-world sfm self-supervision. *IEEE Transactions on Intelligent Transportation Systems*, 2021.

[27] Richard Hartley and Andrew Zisserman. *Multiple view geometry in computer vision*. Cambridge university press, 2003.

[28] Kaiming He, Xiangyu Zhang, Shaoqing Ren, and Jian Sun. Deep residual learning for image recognition. In *Proceedings of the IEEE conference on computer vision and pattern recognition*, pages 770–778, 2016.

[29] Masayuki Kanbara, Takashi Okuma, Haruo Takemura, and Naokazu Yokoya. A stereoscopic video see-through augmented reality system based on real-time vision-based registration. In *Proceedings IEEE Virtual Reality 2000 (Cat. No. 00CB37048)*, pages 255–262. IEEE, 2000.

[30] Alex Kendall, Hayk Martirosyan, Saumitro Dasgupta, Peter Henry, Ryan Kennedy, Abraham Bachrach, and Adam Bry. End-to-end learning of geometry and context for deep stereo regression. In *Proceedings of the IEEE international conference on computer vision*, pages 66–75, 2017.

[31] Wan-Soo Kim, Dae-Hyun Lee, Yong-Joo Kim, Taehyeong Kim, Won-Suk Lee, and Chang-Hyun Choi. Stereo-vision-based crop height estimation for agricultural robots. *Computers and Electronics in Agriculture*, 181:105937, 2021.

[32] Yevhen Kuznetsov, Jorg Stuckler, and Bastian Leibe. Semi-supervised deep learning for monocular depth map prediction. In *Proceedings of the IEEE conference on computer vision and pattern recognition*, pages 6647–6655, 2017.

[33] Jin Han Lee, Myung-Kyu Han, Dong Wook Ko, and Il Hong Suh. From big to small: Multi-scale local planar guidance for monocular depth estimation. *arXiv preprint arXiv:1907.10326*, 2019.

[34] Hanhan Li, Ariel Gordon, Hang Zhao, Vincent Casser, and Anelia Angelova. Unsupervised monocular depth learning in dynamic scenes. In *Conference on Robot Learning*, pages 1908–1917. PMLR, 2021.

[35] Shao-Yuan Lo, Wei Wang, Jim Thomas, Jingjing Zheng, Vishal M Patel, and Cheng-Hao Kuo. Learning feature decomposition for domain adaptive monocular depth estimation. *arXiv preprint arXiv:2208.00160*, 2022.

[36] Robert McCraith, Lukas Neumann, and Andrea Vedaldi. Calibrating self-supervised monocular depth estimation. *arXiv preprint arXiv:2009.07714*, 2020.

[37] Jaswanth Nidamanuri, Chinmayi Nibhanupudi, Rolf Assfalg, and Hrishikesh Venkataraman. A progressive review: Emerging technologies for adas driven solutions. *IEEE Transactions on Intelligent Vehicles*, 7(2):326–341, 2021.

[38] René Ranftl, Katrin Lasinger, David Hafner, Konrad Schindler, and Vladlen Koltun. Towards robust monocular depth estimation: Mixing datasets for zero-shot cross-dataset transfer. *IEEE transactions on pattern analysis and machine intelligence*, 44(3):1623–1637, 2020.

[39] Mark Sandler, Andrew Howard, Menglong Zhu, Andrey Zhmoginov, and Liang-Chieh Chen. Mobilenetv2: Inverted residuals and linear bottlenecks. In *Proceedings of the IEEE conference on computer vision and pattern recognition*, pages 4510–4520, 2018.

[40] Shuwei Shao, Zhongcai Pei, Weihai Chen, Baochang Zhang, Xingming Wu, Dianmin Sun, and David Doermann. Self-supervised learning for monocular depth estimation on minimally invasive surgery scenes. In *2021 IEEE International Conference on Robotics and Automation (ICRA)*, pages 7159–7165. IEEE, 2021.

[41] Kunal Swami, Amrit Muduli, Uttam Gurram, and Pankaj Bajpai. Do what you can, with what you have: Scale-aware and high quality monocular depth estimation without real world labels. In *Proceedings of the IEEE/CVF Conference on Computer Vision and Pattern Recognition*, pages 988–997, 2022.

[42] Jonas Uhrig, Nick Schneider, Lukas Schneider, Uwe Franke, Thomas Brox, and Andreas Geiger. Sparsity invariant cnns. In *2017 international conference on 3D Vision (3DV)*, pages 11–20. IEEE, 2017.

[43] Jamie Watson, Michael Firman, Gabriel J Brostow, and Daniyar Turmukhambetov. Self-supervised monocular depth hints. In *Proceedings of the IEEE/CVF International Conference on Computer Vision*, pages 2162–2171, 2019.

[44] Jamie Watson, Oisin Mac Aodha, Victor Prisacariu, Gabriel Brostow, and Michael Firman. The temporal opportunist: Self-supervised multi-frame monocular depth. In *Proceedings of the IEEE/CVF Conference on Computer Vision and Pattern Recognition*, pages 1164–1174, 2021.

[45] Yi Xiao, Felipe Codevilla, Akhil Gurram, Onay Urfalioglu, and Antonio M López. Multimodal end-to-end autonomous driving. *IEEE Transactions on Intelligent Transportation Systems*, 23(1):537–547, 2020.

[46] Feng Xue, Guirong Zhuo, Ziyuan Huang, Wufei Fu, Zhuoyue Wu, and Marcelo H Ang. Toward hierarchical self-supervised monocular absolute depth estimation for autonomous driving applications. In *2020 IEEE/RSJ International Conference on Intelligent Robots and Systems (IROS)*, pages 2330–2337. IEEE, 2020.

[47] Sen Zhang, Jing Zhang, and Dacheng Tao. Towards scale-aware, robust, and generalizable unsupervised monocular depth estimation by integrating imu motion dynamics. In *European Conference on Computer Vision*, pages 143–160. Springer, 2022.

[48] Shanshan Zhao, Huan Fu, Mingming Gong, and Dacheng Tao. Geometry-aware symmetric domain adaptation for monocular depth estimation. In *Proceedings of the IEEE/CVF Conference on Computer Vision and Pattern Recognition*, pages 9788–9798, 2019.

[49] Chuanxia Zheng, Tat-Jen Cham, and Jianfei Cai. T2net: Synthetic-to-realistic translation for solving single-image depth estimation tasks. In *Proceedings of the European conference on computer vision (ECCV)*, pages 767–783, 2018.

[50] Tinghui Zhou, Matthew Brown, Noah Snavely, and David G Lowe. Unsupervised learning of depth and ego-motion from video. In *Proceedings of the IEEE conference on computer vision and pattern recognition*, pages 1851–1858, 2017.

One scalar is all you need - absolute depth estimation using monocular self-supervision - Supplementary material

Alexandra Dana

Nadav Carmel

Amit Shomer

Ofer Manela

Tomer Peleg

Samsung

Samsung Israel R&D Center, Tel Aviv, Israel

alex.dana@samsung.com

S1. Methods

S1.1. Local motion filtering

Monocular depth estimators (MDEs) trained using self-supervision from image pairs collected at different times are highly sensitive to local motion [4], which breaks the scene stationarity assumption, invalidating Eq. (1) on such regions (see Section 3.1 in the main text). In this work, we suggested to filter non-stationary vehicles from the training data by directly exploiting this self-supervised training weakness. Specifically, we calculated the relative depth on dynamic objects, such as cars, with respect to stationary segments such as the road. On moving objects the relative depth should significantly differ when predicted by a self-supervised MDE that is sensitive to local motion *vs.* an MDE that is fully-supervised and does not suffer from this weakness.

To this end, we first trained the MDE using self-supervision as described in Section 3.5 in the main text. We used this network to infer up-to-scale depths on all the training dataset, creating d_{unsup}^i estimations (i represents the index of an image). Then, we trained the same depth estimation network Φ using full-supervision with a simple L1 loss (see details in Section 3.7, main text) on the *source* training dataset that has available GT depth measurements. We used this network to infer the depth of images from the source and the target training datasets, creating d_{sup}^i estimations. The fully-supervised training is not strictly required and any fully-supervised model can be used, as long as it can generalize well enough to produce continuous depth maps on roads and cars (without necessarily resulting in correct depth scaling).

We then utilized a semantic-segmentation network [6] to detect the road region and scaled both d_{sup}^i and d_{unsup}^i by dividing them with their respective *road-pixels* median, resulting in $d_{sup-scaled}^i$ and $d_{unsup-scaled}^i$ estimations.

Next, we employed an off-the-shelf instance-level seg-

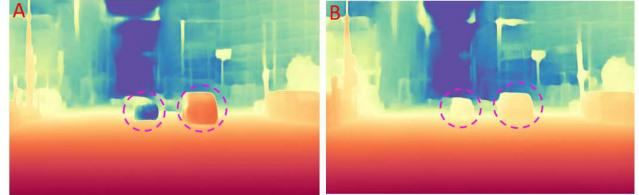


Figure S1. Demonstrating the effect of local motion on self-supervised training (inferred image taken from the DDAD1 dataset). A. The resulting depth estimation map when the MDE was trained using self-supervision with limited local motion filtering [4]. B. The depth estimation map after applying our additional local motion masks on potentially moving vehicles during training. Dashed circles are located on moving cars in opposite directions (left/right car is moving from/towards the ego-car).

mentation network to estimate the location of vehicles [8]. For each vehicle we calculated the absolute difference $|d_{sup-scaled}^i - d_{unsup-scaled}^i|$ values, setting a local-motion cutoff value above C for at least $R\%$ of each vehicle pixels. In this work we empirically set C to 1.5 (reflecting $d_{unsup-scaled}^i$ depth deviations of more than 50% with respect to $d_{sup-scaled}^i$) and R to 10 (reflecting that at least 10% of pixels are affected by local motion).

We repeated the self-supervised training of models Φ and Ψ using the additionally created local-motion masks. These step reduced areas that violated the static scene assumption, which in turn improved poor estimations on moving objects. An example of the resulting local motion filtering applied during training is shown in Figure S1.

S1.2. Depth evaluation metrics

We calculated the absolute relative depth metric (*AbsRel*) as previously described [2]:

$$AbsRel = \frac{1}{T} \sum_t^T \frac{1}{N_t} \sum_n^{N_t} \left(\left| \frac{depth_{pred}^{t,n} - depth_{GT}^{t,n}}{depth_{GT}^{t,n}} \right| \right) \quad (1)$$

where n denotes pixels with valid GT depths, N_t the number of pixels with valid GT depth in image t and T the number of images in the test dataset.

To measure the *AbsRel* of predicted up-to-scale depths, predicted up-to-scale depths of image t were first normalized using the ratio α between the median of the predicted and the GT depth values (per image) [9], resulting in *AbsRel_{norm}*.

$$AbsRel_{norm} = \frac{1}{T} \sum_t^T \frac{1}{N_t} \sum_n^{N_t} \left(\left| \frac{\alpha depth_{pred}^{t,n} - depth_{GT}^{t,n}}{depth_{GT}^{t,n}} \right| \right) \quad (2)$$

$$\text{where } \alpha = \frac{\text{median}(depth_{GT}^{t,n})}{\text{median}(depth_{pred}^{t,n})}.$$

To assess scaling similarity we also calculated the median ratio between the predicted absolute depths and the GT depths per image, and then averaged this value across the entire test dataset, resulting in *scale_{ratio}*:

$$scale_{ratio} = \frac{1}{T} \sum_t^T \text{median} \left(\frac{depth_{pred}^{t,n}}{depth_{GT}^{t,n}} \right) \quad (3)$$

S1.3. Datasets

KITTI. This dataset [3] is considered the standard benchmark for depth evaluation. Its Eigen split [2] resulted in 39,810 training images, 4,424 validation and 697 evaluation images. This dataset was recorded during various days and the stereo rectification resulted in slight FOV variability between 81.43° and 82.68°. The cameras were located 1.65 m above the ground.

To enable comparison to previous works, we evaluated our method on the 697 Eigen split evaluation images (see main text, Table 5). In the rest of the paper we reported accuracy on the newer Eigen Benchmark evaluation dataset [7], which has an improved ground truth depth and contains 652 evaluation images. To ease the reading flow, we refer to the evaluation dataset as the test dataset. The FOVs of datasets that were used as a source domain to KITTI were adjusted to 81.43°.

DDAD. This depth evaluation benchmark [5] was collected from various locations in the world using six cameras (front, rear, sides). The training dataset contains 12,560 images and the validation dataset contains 3,950 images (per camera). To ease the reading flow, in this work we refer

to the validation dataset as our test dataset. The front camera has a FOV between 47.66° and 48.26°, while the rear camera has a FOV between 82.21° and 84.46°. All cameras were located 1.49-1.54 m above the ground. We refer to data collected using the front and the rear cameras as DDAD1 and DDAD9 respectively, following the dataset camera numbering convention. The FOVs of all datasets that were used as a source domain to DDAD1 were adjusted to 47.85°.

vKITTI2. This synthetic dataset [1] was recently released as a more photo-realistic version of vKITTI [3], containing reconstructions of five sequences found in the KITTI odometry benchmark with full-pixel ground truth. We used only camera 0 from all scenes and all of its rotations ±15° and ±30°, from the clear day simulation, resulting in 9,560 images. From each sequence and rotation angle we used the first 90% of images for training and the rest for testing purposes. Similarly to KITTI, the FOV of the images in this dataset is 81.16°, created using a camera located ∼1.58 m above the ground.

In this work we defined the DDAD1 and KITTI as target datasets. For the DDAD1 target domain we used KITTI and vKITTI2 as source domains. For the KITTI target domain we used vKITTI and DDAD9 as source domains (DDAD1 FOV is too small). When the applied FOV adjustment (see Section 3.2 in the main text) resulted in crops larger than the original image (e.g. KITTI FOV correction to DDAD1), these sections were filled using reflection/zero padding for images/GT depth. In experiments where KITTI was defined as the target domain, input images for the various trained networks were resized to 320x1024. When DDAD1 was defined as the target domain, the input images for the various trained networks were resized to 608x960. We cap the depth range to 80 m during evaluation for both KITTI and the DDAD1 target datasets.

S2. Results

S2.1. Aligning images from different domains to the same size

We present additional scatter plots of the naïve resizing of DDAD source images (see Section 4.3 in the main text), instead of applying our suggested FOV adjustment to match the target KITTI image sizes. Figure S2 shows the obtained GT to up-to-scale depth scatter plots after self-supervised training on mixed batches of images from the target and source domain (after applying the naïve resizing methods on the source images).

S2.2. Demonstrating depth ranking linearity on another architecture

We hypothesized that the depth linear ranking property observed in self-supervised MDEs is independent of

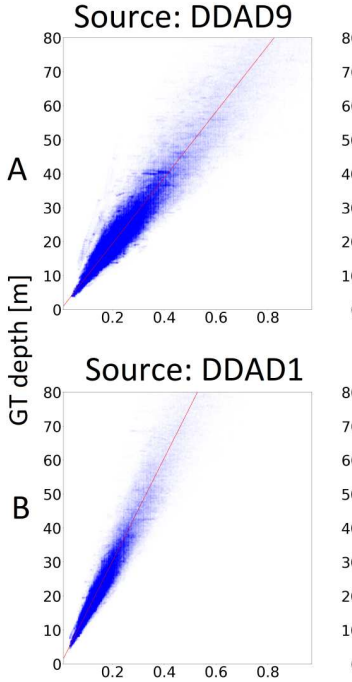


Figure S2. Naïve resizing of source images to the size of target images using the two different approaches (A) and (B) described in Section 4.3. Up-to-scale depths were inferred using an MDE that was trained using self-supervision on batches with mixed source and target images. Source images were adjusted using the suggested naïve resizing methods. GT to up-to-scale depth scatter plots were calculated on the source and the target test datasets.

their architecture, but determined by the used training loss. To this end, we analyzed depth predictions of the PackNet architecture [5]. This architecture utilizes 3D convolutions and significantly differs from our encoder-decoder architecture, but uses a similar training loss as our self-supervised training regime. In their work, the authors predicted 1/depth, thus the up-to-scale depth values are not limited to 1. We inferred depth predictions on the DDAD1 dataset using the publicly available PackNet model, which was trained using self-supervision on 384x640 resized images from the same domain. Figure S3 demonstrates the linear relationship between the GT and predicted up-to-scale depths of this network, achieving a Pearson coefficient of $p=0.8$ on all predictions and $p=0.97$ on predictions with $AbsRel_{norm} < 15\%$, reinforcing our assumption.

S2.3. Transferring depth scale from the source to the target domain - additional metrics

We evaluated the global depth-scale transfer method and the per-image depth-scale network Γ using additional depth accuracy metrics and reported them in Tables S1, S2. Figures S4-S7 show inferred up-to-scale depths from the source and the target domain, when separately training the MDE

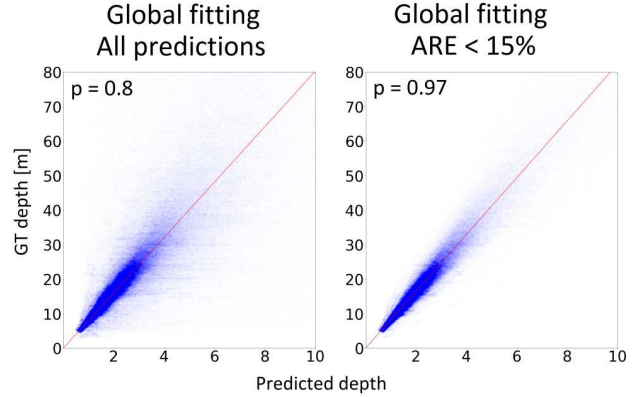


Figure S3. GT to up-to-scale predicted depth estimations using the PackNet architecture. Left: all predictions. Right: predictions with $AbsRel_{norm} < 15\%$. The fitting line was calculated using Eq. (5) in the main text and depicted with a red line. The calculated Pearson coefficient (p) was added for each scatter plot.

using self-supervision on each one of the domains (upper row) and up-to-scale depths after training the MDE on mixed-batches from both the source and the target domains (bottom row). FOV of source images in both cases was adjusted to the target FOV. Self-supervised training on mixed batches from different domains was shown to not qualitatively degrade the estimated depth maps.

References

- [1] Yohann Cabon, Naila Murray, and Martin Humenberger. Virtual kitti 2, 2020. [S2](#)
- [2] David Eigen, Christian Puhrsch, and Rob Fergus. Depth map prediction from a single image using a multi-scale deep network. *Advances in neural information processing systems*, 27, 2014. [S2](#)
- [3] A Gaidon, Q Wang, Y Cabon, and E Vig. Virtual worlds as proxy for multi-object tracking analysis. In *CVPR*, 2016. [S2](#)
- [4] Clément Godard, Oisin Mac Aodha, Michael Firman, and Gabriel J Brostow. Digging into self-supervised monocular depth estimation. In *Proceedings of the IEEE/CVF international conference on computer vision*, pages 3828–3838, 2019. [S1](#)
- [5] Vitor Guizilini, Rares Ambrus, Sudeep Pillai, Allan Raventos, and Adrien Gaidon. 3d packing for self-supervised monocular depth estimation. In *Proceedings of the IEEE/CVF conference on computer vision and pattern recognition*, pages 2485–2494, 2020. [S2](#), [S3](#)
- [6] Andrew Tao, Karan Sapra, and Bryan Catanzaro. Hierarchical multi-scale attention for semantic segmentation. *arXiv preprint arXiv:2005.10821*, 2020. [S1](#)
- [7] Jonas Uhrig, Nick Schneider, Lukas Schneider, Uwe Franke, Thomas Brox, and Andreas Geiger. Sparsity invariant cnns. In *2017 international conference on 3D Vision (3DV)*, pages 11–20. IEEE, 2017. [S2](#), [S5](#)

- [8] Yuxin Wu, Alexander Kirillov, Francisco Massa, Wan-Yen Lo, and Ross Girshick. Detectron2. <https://github.com/facebookresearch/detectron2>, 2019. **S1**
- [9] Tinghui Zhou, Matthew Brown, Noah Snavely, and David G Lowe. Unsupervised learning of depth and ego-motion from video. In *Proceedings of the IEEE conference on computer vision and pattern recognition*, pages 1851–1858, 2017. **S2**

Table S1. Depth-scale-transfer implemented using our global depth-scaling scalar G_{dscale} . For KITTI, metrics were calculated on the Eigen benchmark evaluation data [7].

Target	Source	Lower is better ↓					Higher is better ↑			$Scale_{ratio}$
		$AbsRel$	$AbsRel_{norm}$	Sq Rel	RMSE	$RMSE_{log}$	$\delta < 1.25$	$\delta < 1.25^2$	$\delta < 1.25^3$	
KITTI	DDAD9	0.084	0.076	0.418	3.567	0.125	0.924	0.987	0.997	1.03±0.05
	vKITTI2	0.096	0.077	0.572	3.869	0.131	0.924	0.988	0.996	1.04±0.06
DDAD1	KITTI	0.128	0.119	1.533	7.337	0.204	0.850	0.956	0.982	0.95±0.05
	vKITTI2	0.137	0.135	1.959	8.548	0.218	0.817	0.943	0.978	1.01±0.05

Table S2. Depth-scale-transfer implemented using our per-image depth-scale network Γ . For KITTI, metrics were calculated on the Eigen benchmark evaluation data [7].

Target	Source	Lower is better ↓					Higher is better ↑			$Scale_{ratio}$
		$AbsRel$	$AbsRel_{norm}$	Sq Rel	RMSE	$RMSE_{log}$	$\delta < 1.25$	$\delta < 1.25^2$	$\delta < 1.25^3$	
KITTI	DDAD9	0.091	0.075	0.44	3.665	0.132	0.913	0.986	0.997	0.97±0.06
	vKITTI2	0.101	0.076	0.513	3.601	0.132	0.922	0.988	0.997	1.05±0.06
DDAD1	KITTI	0.135	0.118	1.554	7.405	0.208	0.844	0.955	0.982	0.94±0.06
	vKITTI2	0.169	0.134	2.200	8.693	0.224	0.802	0.947	0.979	1.08±0.07

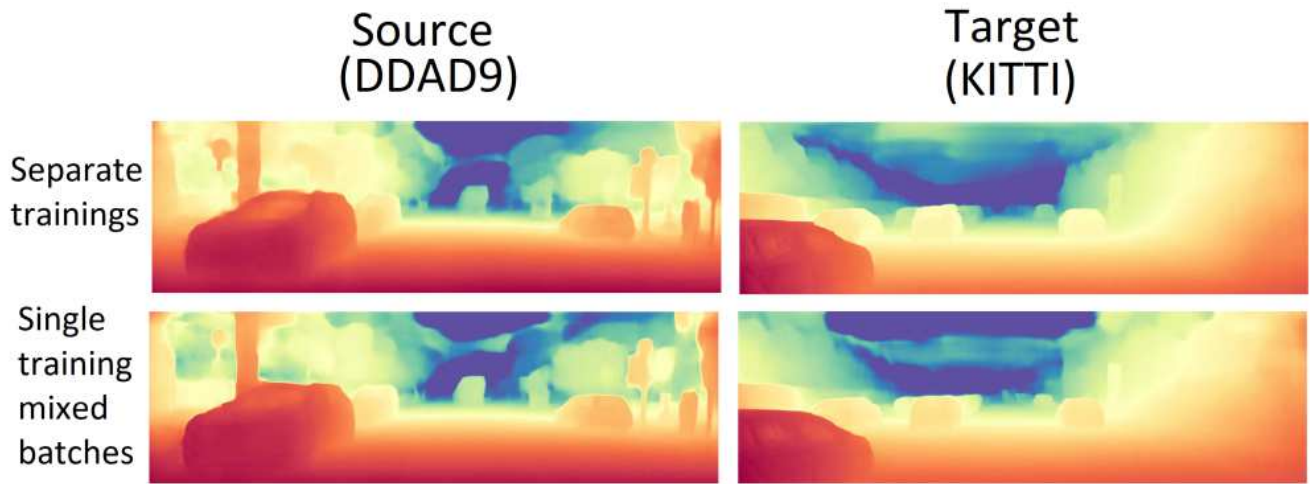


Figure S4. Upper row: two MDEs are separately trained using self-supervision on DDAD9 and KITTI. Bottom row: One MDE is trained using self-supervision on mixed batches from DDAD9 and KITTI. In both experiments the FOV of DDAD9 images was adjusted to the KITTI FOV.

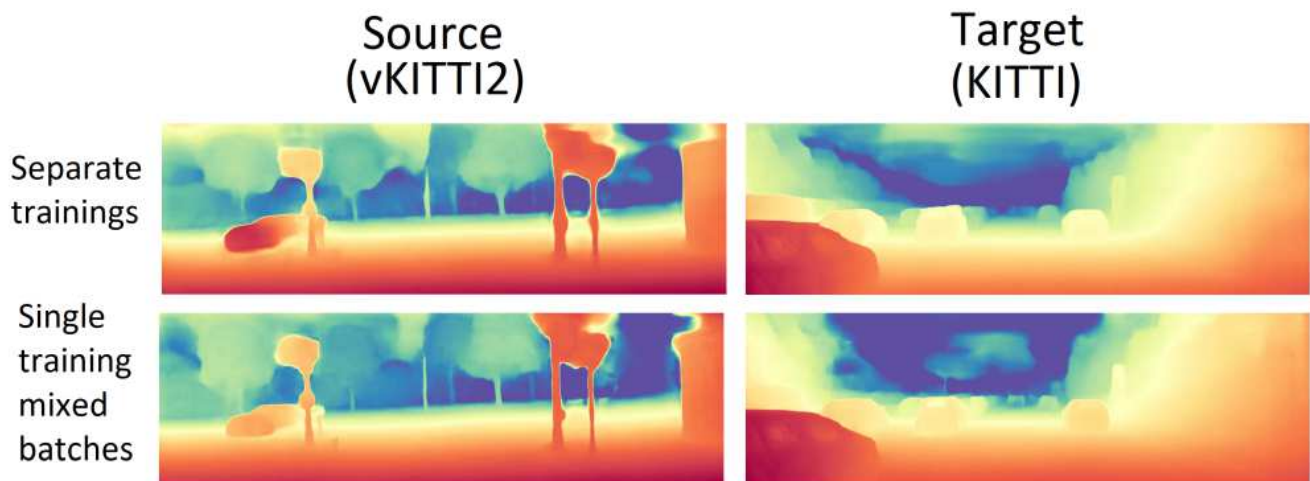


Figure S5. Upper row: two MDEs are separately trained using self-supervision on vKITTI2 and KITTI. Bottom row: One MDE is trained using self-supervision on mixed batches from vKITTI2 and KITTI.

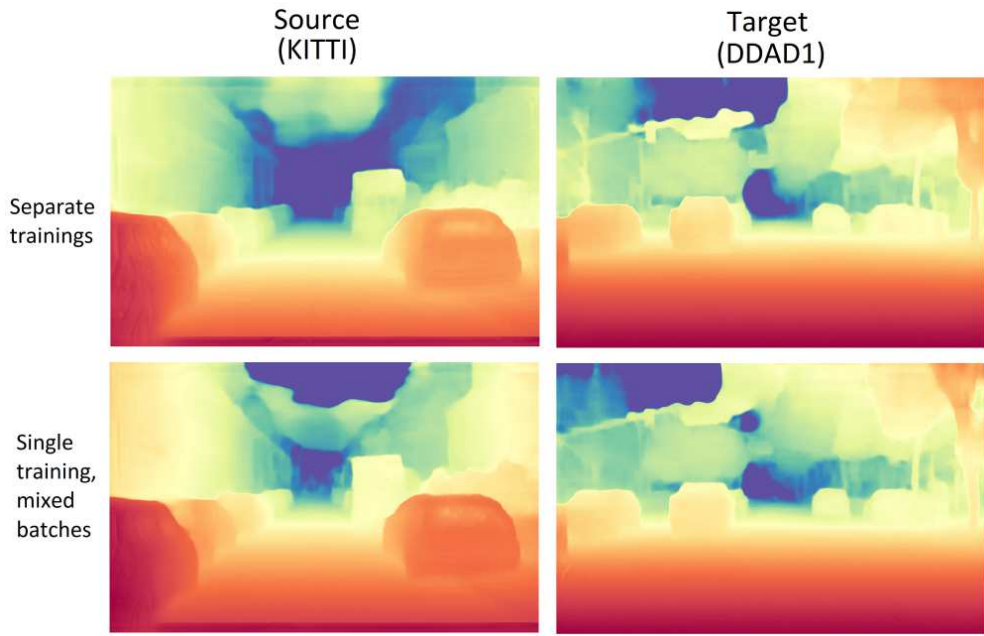


Figure S6. Upper row: two MDEs are separately trained using self-supervision on KITTI and DDAD1. Bottom row: One MDE is trained using self-supervision on mixed batches from KITTI and DDAD1. In both experiments the FOV of KITTI images was adjusted to the DDAD1 FOV.

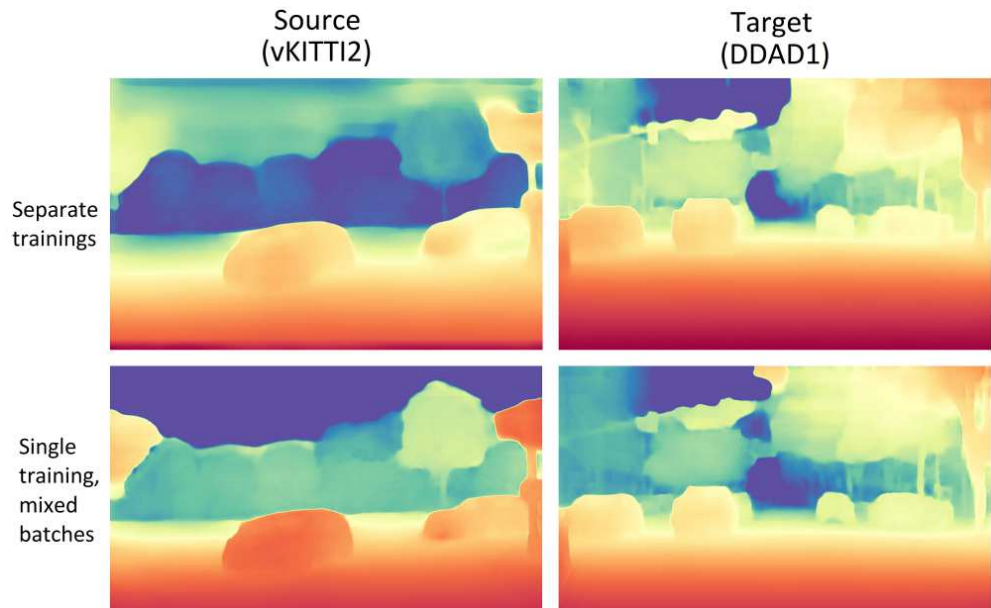


Figure S7. Upper row: two MDEs are separately trained using self-supervision on vKITTI2 and DDAD1. Bottom row: One MDE is trained using self-supervision on mixed batches from vKITTI2 and DDAD1. In both experiments the FOV of vKITTI2 images was adjusted to the DDAD1 FOV.